J Mater Sci: Mater Electron (2013) 24:4790–4797
DOI 10.1007/s10854-013-1476-8

J_c enhancement and flux pinning of Se substituted YBCO compound

Z. D. Yakinci · D. M. Gokhfeld · E. Altin · F. Kurt · S. Altin · S. Demirel · M. A. Aksan · M. E. Yakinci

Received: 19 June 2013 / Accepted: 27 August 2013 / Published online: 13 September 2013

Abstract $Y_{2/3}$ $Se_{1/3}Ba_2Cu_3O_x$ compound was fabricated by using solid state fabrication technique. Optimum heat treatments conditions for $Y_{0.77}Se_{0.33}Ba_2Cu_3O_x$ were investigated. It was determined that the XRD results of these samples were similar to Y-123 phase with some impurities. Magnetization dependence of applied magnetic fields was measured in the range of 0–9 T at 10–50 K. The symmetric and asymmetric *M–H* loops were obtained for the samples. Magnetization loops obtained from measurements were successfully described by the extended Valkov–Khrustalev model. The temperature and applied magnetic field dependencies of magnetization of sample were estimated and critical current density of samples was calculated by Bean model and pinning force of samples was calculated by using Lorentz force. It is found from critical current density values that Se additions were acted as a pinning center which increased critical current density.

Z. D. Yakinci
Saglik Hizmetleri Meslek Yuksek Okulu, Inonu Universitesi, 44280 Malatya, Turkey

D. M. Gokhfeld
L.V. Kirensky Institute of Physics, SB RAS, 660036 Krasnoyarsk, Russia

E. Altin · F. Kurt · S. Demirel (✉)
Bilimsel ve Teknolojik Arastrma Merkezi, Inonu Universitesi, 44280 Malatya, Turkey
e-mail: demirel.srkn@gmail.com

S. Altin · M. A. Aksan · M. E. Yakinci
İnonu Universitesi, Fen Edebiyat fakultesi, Superiletkenlik Arastirma Grubu, Inonu Universitesi, 44280 Malatya, Turkey

1 Introduction

After discovery of superconductivity in the $YBa_2Cu_3O_{7-\delta}$ (YBCO) system above liquid nitrogen temperature (77 K) [1], scientists have spent much effort to increase the superconducting transition temperature, T_c, and critical current, J_c. For this purpose, different preparation techniques, dopings/substitutions and additions to the system were performed.

Three different phases are presented in the YBCO system: Y-123, Y-124 and Y-247 with the T_c values at 90, 80 and 80 K, respectively [2–5]. Y-123 system has a special importance due to high current carrying capacity at 77 K and high critical magnetic field, H_c [6, 7]. J_c of the system strongly depends on the Cu-chains which control the carrier density at the CuO planes [8] and so the T_c value [9, 10]. It is expected that the increasing CuO planes in unit cell can cause an increase in the T_c value of the system. However, the highest T_c value was obtained only in Y-123.

The superconducting properties depend strongly on stoichiometry of the HT_c YBCO system. Small changes in the stoichiometry, especially deficiency of Ba and Cu, can significantly influence the properties of YBCO. Yoshikate et al. investigated the Cu deficiency in the YBCO system. They found that the crystal structure changed significantly even with small change in the copper content of system and thus the superconducting properties was deteriorated [11]. Vasillev et al. [12] found that the change in the Ba and Cu contents of the system caused the change of the oxygen content and so the superconducting properties. Hattori et al. [13] studied the correlation between superconductivity and the Ba and Cu content. They found that the change of the Cu content from 3.26 to 2.82 with a small difference in the Ba content can cause the increase on room temperature resistivity and lead to the suppressed T_c value. Schneider

et al. investigated the effect of Ba/Y ratio on T_c. They reported that the Ba/Y ratio between 0.5 and 2.4 did not have important effect on the T_c value but T_c decreased above 2.4. The highest J_c was obtained when the ratio was 1.8 [14].

There are limited studies on the Se doped/substituted YBCO system [15–17]. In the studies, it was found that the Se substitution decreased drastically T_c and changed the unit cell of $YBa_2Cu_3O_7$ from orthorhombic to tetragonal. The c-axis decreased compared to undoped YBCO system.

In this paper, the samples with stoichiometry of $Y_{2/3}$ $Se_{1/3}Ba_2Cu_3O_x$ were fabricated by conventional solid-state reaction technique. Structural/microstructural analyses of the samples were investigated by XRD, SEM-EDX. Electrical property of the samples was examined by *R–T* measurements. Magnetic properties, the critical current density and pinning properties of the samples were analyzed in the present paper.

2 Experimental details

The samples were prepared using solid-state reaction technique. High purity powders of Y_2O_3, SeO_2, $BaCO_3$ and CuO were weighted in the appropriate amounts to give nominal composition of $Y_{2/3}$ $Se_{1/3}Ba_2Cu_3O_x$. The powders were mixed using an agate mortar and then calcined at 900 °C for 24 h with intermediate grinding and mixing. After calcination, the powders were pressed into pellets at 4 tons. The pellets were sintered at temperatures between 900 and 980 °C for 24 h under oxygen atmosphere. It was seen that the samples heat treated at 980 °C were melted.

The structural characterization of the samples was performed by X-ray diffraction (XRD). Scan speed was selected as $2°\ min^{-1}$ in the range of $2\theta = 20°–80°$. Automated Rigaku RadB Dmax X-ray diffractometer with CuK_α radiation was used for the XRD analysis.

The microstructural and compositional characterization of the materials were carried out with Leo EVO-40 XVP scanning electron microscope (SEM) and BRUKER X-flash detector 4010 energy dispersive x-ray spectroscope (EDX).

Temperature dependence of resistivity ($\rho-T$) of the samples fabricated was investigated by closed cycle Leybold LT-10 cryostat system combined with SRS ac bridge system using 17.7 Hz frequency. For resistivity measurements, the four probe electrical contacts were made by silver paste. The T_c values of samples fabricated were determined by the resistivity differentiation $d\rho(T)/dT$. The peak temperature in $d\rho(T)/dT$ plot was defined as the T_c value. *M–T* and *M–H* measurements were performed using Quantum Design PPMS system at 10, 20, 30, 40 and 50 K up to 9 T. Critical current density, J_c, was calculated with Bean model for all samples at 10–50 K up to 9 T. Pinning force, F_p, depending on temperature and applied magnetic field was calculated using *M–H* data.

3 Results and discussion

3.1 XRD results

The XRD patterns of $Y_{2/3}$ $Se_{1/3}Ba_2Cu_3O_x$, depending on the heat treatment conditions, are given in Fig. 1. The samples heat treated at 900–960 °C for 24 h under O_2 atmosphere consisted mainly of $YBa_2Cu_3O_7$. However, impurity peaks such as $BaSeO_4$ and $CuSe_2O_5$ were also detected, as seen in Fig. 1. The crystal symmetry of the samples was determined as orthorhombic. The unit cell parameters of the samples are listed in Table 1. The results indicated that the calculated unit cell parameters are close to the pure Y-123 system with a small difference [18–20]. We believe that the reason of the difference on the unit cell parameters can be due to occupation of the Se ions to interstitial sites. The interstitial occupation causes the change of the unit cell parameters.

3.2 Micro-structural properties

Surface morphology of the samples fabricated at 900–960 °C for 24 h under O_2 atmosphere is given in Fig. 2a–d. The main matrix of the sample fabricated at 900 °C for 24 h was identified to be Y-123 from the EDX analysis. Some dark regions were observed on the surface of the sample. EDX analysis showed that atomic composition of these dark regions corresponded to $BaSeO_4$ and $CuSe_2O_5$, respectively. Different surface morphology was obtained with increasing the heat treatment temperature, Fig. 2b–d. The partial melted grains on the surface were

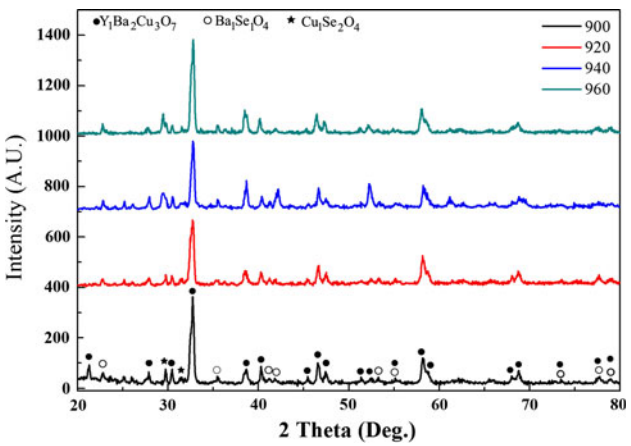

Fig. 1 XRD pattern of $Y_1Se_{0.33}Ba_{1.67}Cu_{2.67}O_x$ compounds depending on heat treatment conditions

Table 1 Crystal parameters of $Y_1Se_{0.33}Ba_{1.67}Cu_{2.67}O_x$ samples depending on heat treatment conditions

Heat treatment temperature (°C)	Main phase	Symmetry	a (Å)	b (Å)	c (Å)
900	Y-123	Orthorhombic	3.824	3.887	11.697
920	Y-123	Orthorhombic	3.826	3.888	11.706
940	Y-123	Orthorhombic	3.827	3.887	11.731
960	Y-123	Orthorhombic	3.816	3.897	11.724

observed on the samples. Especially, size and number of the partially melted grains increased with the heat treatment temperature. The samples were melted for the heat treatment temperatures above 960 °C.

3.3 Electrical properties

Temperature dependence of the electrical resistivity of the samples depending on the heat treatment conditions is presented in Fig. 3. All the samples showed metallic behavior above T_c and the resistivity dropped to zero below T_c. The T_c and T_0 values of the samples heat treated at 900–960 °C are given in Table 2. The highest T_c and T_0 value were obtained to be 94.9 and 90.3 K for the sample heat treated at 920 °C for 24 h. It was seen that normal state resistivity values in the samples heat treated above 920 °C increased compared to the samples fabricated at 900 and 920 °C. It is believed that this increase on the normal state resistivity value is attributed to deterioration of microstructure of the samples with the Se addition and/or with increasing the heat treatment temperature. Particularly, the occupation of the interstitial sites by the Se atoms can be caused the increase of the normal state resistivity of the samples, compared to the undoped YBCO material.

3.4 Magnetic properties

The temperature dependent magnetization was measured from 50 to 100 K under zero magnetic field. The temperature dependence of magnetization of the samples fabricated (M–T) is given in Fig. 4. The highest diamagnetic signal with sharp drop was obtained for the sample fabricated at 920 °C, suggesting strong grain connection in the sample. The onset temperature, T_c^{on}, of diamagnetic signal of the samples is presented in Table 2.

It is known that magnetic behavior of the superconducting materials is associated strongly to previous history of the applied magnetic field. When the applied magnetic field is increased from zero to a specific value and then returned through zero, the hysteresis behavior can be observed. The reason of this irreversible manner of

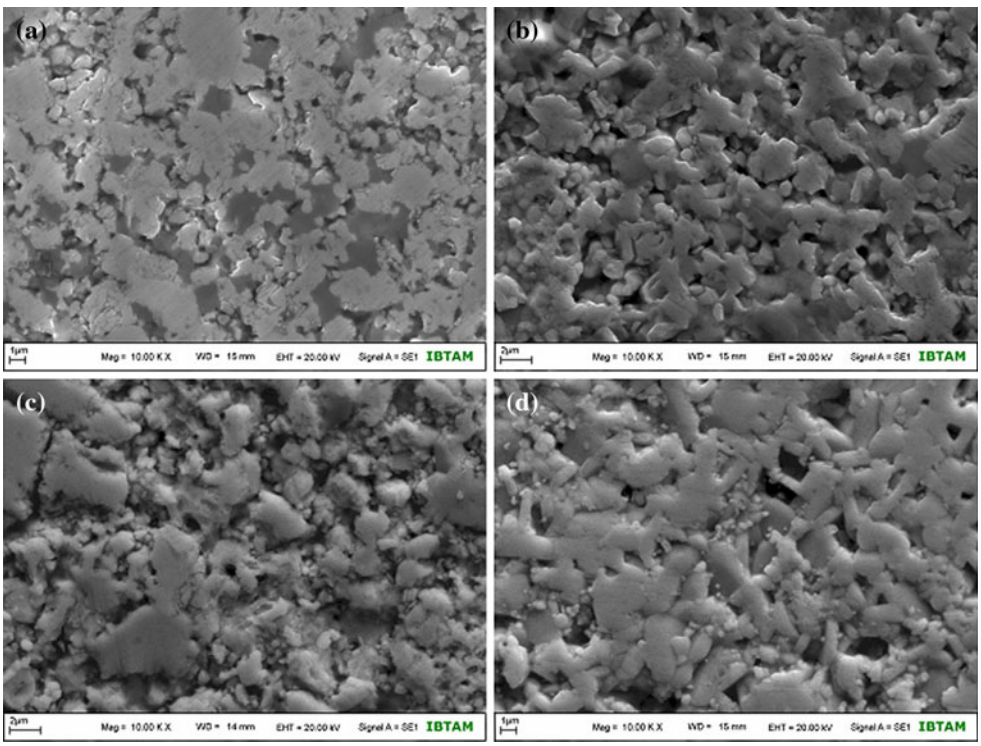

Fig. 2 Surface morphology of samples heat treated at (**a**) 900 °C, (**b**) 920 °C, (**c**) 940 °C and (**d**) 960 °C for 24 h under oxygen atmosphere

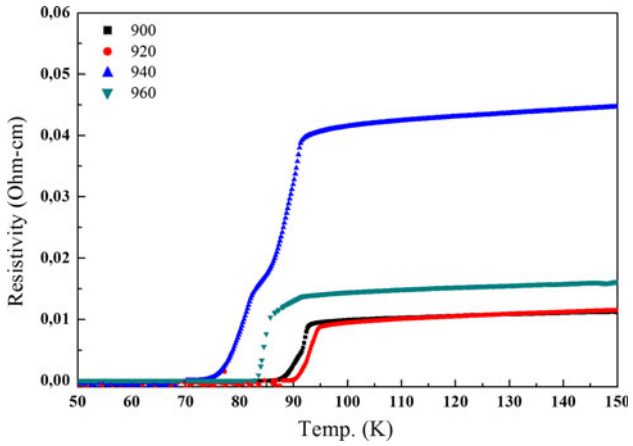

Fig. 3 Temperature dependence of electrical resistivity of the samples fabricated at different heat treatment conditions

Table 2 T_c values of samples obtained from electrical and magnetic measurements depending on heat treatment cycles

Heat treatment temperature (°C)	From electrical resistivity		From magnetization	
	T_c (K)	T_0 (K)	ΔT (K)	T_c^{on} (K)
900	92.9	87.1	5.8	90.7
920	94.3	90.2	4.1	90.9
940	91.7	75.6	16.1	90.6
960	90.8	82.6	8.2	80.4

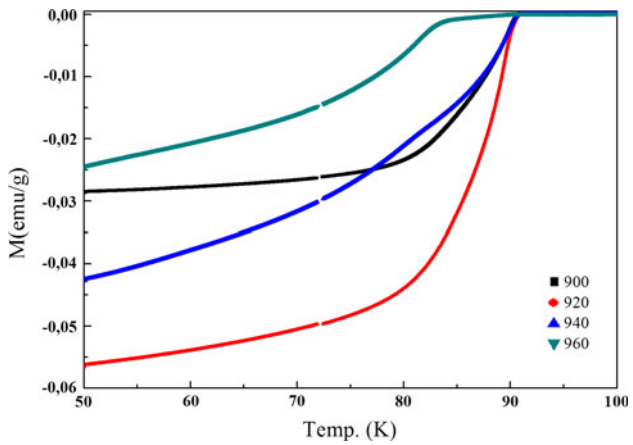

Fig. 4 Temperature dependence of DC-magnetization of the samples fabricated at different heat treatment conditions

magnetization can be due to flux trapping in superconducting samples, which has a crucial importance on critical current density.

Figure 5 shows the *M–H* curves of the samples at five different temperatures (10, 20, 30, 40, 50 K) up to 9 T. In general, the non-symmetric hysteresis was obtained for all the samples. The *M–H* curves decreased rapidly up to ~2 T and then varied smoothly with the magnetic field. The magnetization values for all the samples remained non-zero at 9 T for all the measurement temperatures. The highest zero-field magnetization value was obtained at 10 K for the sample fabricated at 920 °C for 24 h, as seen in Fig. 5b. But, the zero-field magnetization value at 10 K decreased for other samples. We believe that this is related to inter-grain and/or intra-grain magnetic behavior in the samples. Magnetization decreased with increasing the temperature and the applied magnetic field. At low temperatures, the pinning is strong and the flux mostly penetrates a material as the vortices. Magnetization caused by the pinning becomes smaller as temperature increases. The vortex motion in the material starts with increase in the temperature, which leads to deterioration in the magnetic configuration of fluxes [21, 22].

To analyze *M–H* loops, we subtracted the linear paramagnetic contribution which is different for each samples, such that the *M*(*H*) dependencies have become almost independent of *H* at high fields. In contrast to [23, 24], the *M*(*H*) curves at different temperatures cannot be scaled for all the investigated sample. However, the scaling is observed for the *M*(*H*) curves of the different samples at the same temperature. The *M*(*H*) curves of the samples coincide then data are re-plotted at reduced units, M/M_m versus H/H_m, where H_m is the field at which the virgin magnetization curve reaches its minimum M_m. Figures 6 and 7 demonstrate the reduced magnetization M/M_m versus the reduced magnetic field H/H_m at 10 and 50 K for samples treated at 900, 920, 940, 960 °C.

It should be noted that the scaling cannot be reproduced to a parameter. Different scaling along *M* and *H* axes may be due to the inter-granular field compression [25] providing that the magnetic field near grains is larger than the external field.

The extended critical state model [26] combining the Valkov–Khrustalev approach [27] with the critical state model [28] was used to fit the *M–H* loops. The critical current density, J_c, and the depth of the equilibrium surface layer l_s, which are the main fitting parameters, determine the width and the asymmetry of magnetization loop. The fitting parameters at $H = 0$ are presented in Table 3, the depth l_s is compared with the average grain size, *D*.

The critical current density obtained from *M–H* loops, J_c^{mag}, was calculated using Bean's formula [29] given by

$$J_c^{mag} = 20\frac{\Delta M}{a(1 - a/3b)}, \quad (1)$$

where $\Delta M = M^+ - M^-$ is the width of magnetization hysteresis, a and b ($a < b$) are the dimensions of the samples. The applied magnetic field dependence of J_c^{mag}, ($J_c^{mag} - H$), at 10, 20, 30, 40 and 50 K for the samples heat treated at 900, 920, 940 and 960 °C is presented in Fig. 8. The maximum J_c^{mag} value was calculated to be

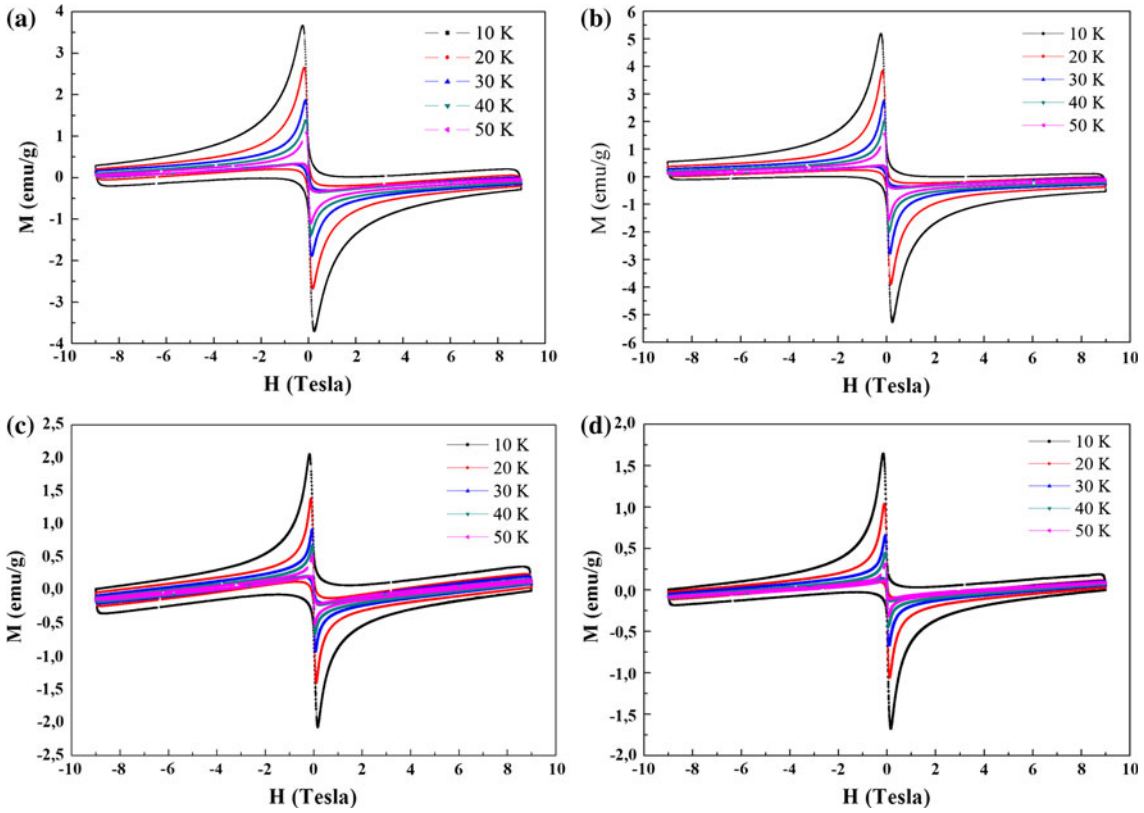

Fig. 5 Magnetic hysteresis loops depending on temperature of the samples heat treated at (**a**) 900 °C, (**b**) 920 °C, (**c**) 940 °C and (**d**) 960 °C for 24 h under oxygen atmosphere

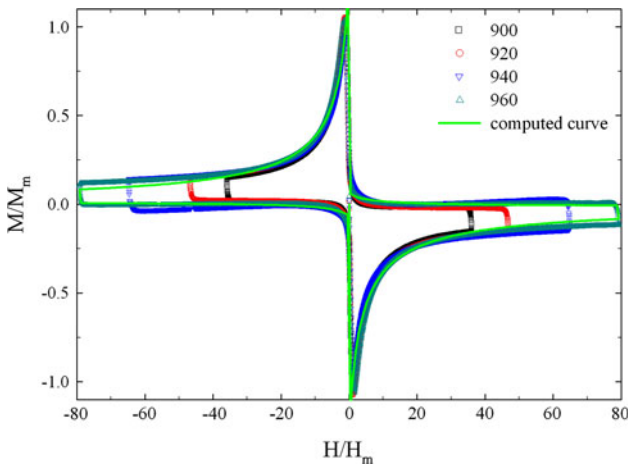

Fig. 6 Scaling of magnetization at $T = 10$ K. Reduced magnetization $M'M_m$ versus reduced magnetic field H/H_m

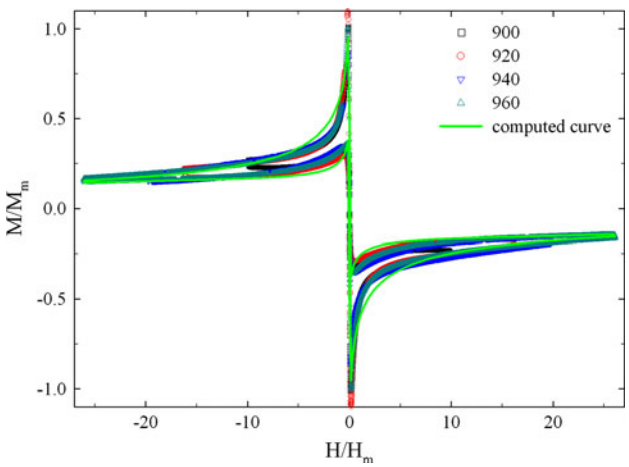

Fig. 7 Scaling of magnetization at $T = 50$ K. Reduced magnetization $M'M_m$ versus reduced magnetic field H/H_m

9.76×10^5 A cm^{-2} at 10 K for magnetic field of 0 T for the sample fabricated at 920 °C for 24 h. The J_c^{mag} values dropped with increasing the applied magnetic field and also temperature as seen in Fig. 8a–d. J_c^{mag} for all the samples showed a plateau after the magnetic field of 1 T. We believe that intrinsic pinning of flux can be responsible for the plateau in the $J_c^{mag} - H$ plots. The J_c^{mag} values of $Y_1Se_{0.33}Ba_{1.67}Cu_{2.67}O_x$ samples are higher than that of undoped Y-123 system [30]. This result indicated that the Se adding and also Ba and Cu deficiencies in YBCO act as the pinning centers and increased the J_c^{mag} value of the YBCO system.

When a current density, J_c, is passed through a superconductor below T_c, an electromagnetic interaction force

Table 3 Scaling coefficients H_m, M_m and fitting parameters J_c, $2l_s/D$ for $M(H)$ curves at $T = 10$ and 50 K

Heat treatment temperature (°C)	T (K)	H_m (T)	M_m (emu/cm^3)	$J_c \times 10^6$ (A/cm^2)	$2l_s/D$
900	10	2.5	19.3	45	0.19
	50	1	5.9	14	0.33
920	10	1.9	21.4	50	0.19
	50	0.56	6.2	14.7	0.33
940	10	1.4	5.5	13	0.19
	50	0.46	1.5	3.6	0.33
960	10	1.1	5.4	12.5	0.19
	50	0.35	1.1	2.5	0.33

emerges between fluxoids and the carriers which are responsible for the current. The Lorentz force, F_L, [31] is

$$F_L = J \times B, \quad (2)$$

where J_c is the current density and B the flux density in the sample. Fluxoids remain stationary and the superconducting behavior of the material maintains with zero resistance as long as the pinning force, F_p, equals at least to F_L. When F_L acting the floxids exceeds F_p, the floxids begin to move across the sample and the material becomes resistive. In that case, the current is no longer without loss. Figure 9 shows the magnetic field dependence of bulk pinning force, F_p, of the samples at five different temperatures. It was found that F_p decreased with increasing the temperature. The maximum value of F_p was calculated to be 5.7×10^4 N/cm^3 at 10 K for the sample heat treated at 900 °C for 24 h, as seen in Fig. 9a. F_p with the applied magnetic field showed almost similar behavior for all the samples. Any peak in F_p was not observed at temperatures of 20 and 50 K and F_p increased almost linear up to 9 T. The maximum values of F_p at 10 K are found to be 5.1×10^4 N/cm^3, 7.1×10^3 N/cm^3 and 1.75×10^3 N/cm^3 for the sample fabricated at 920, 940 and 960 °C, respectively.

To understand the pinning mechanism in the samples, the behavior of flux line lattice (FLL) and pinning centers in the sample should be considered. If the interaction force among flux lines is higher than F_p, FLL is elastically stiff and the correlated flux grain size is large, which means that the bulk F_p is small. On the other hand, if F_p increases relative to the inter-flux line forces, the correlated grains become smaller and approach a limited grain size equal to average pinning center spacing, so that each flux lattice

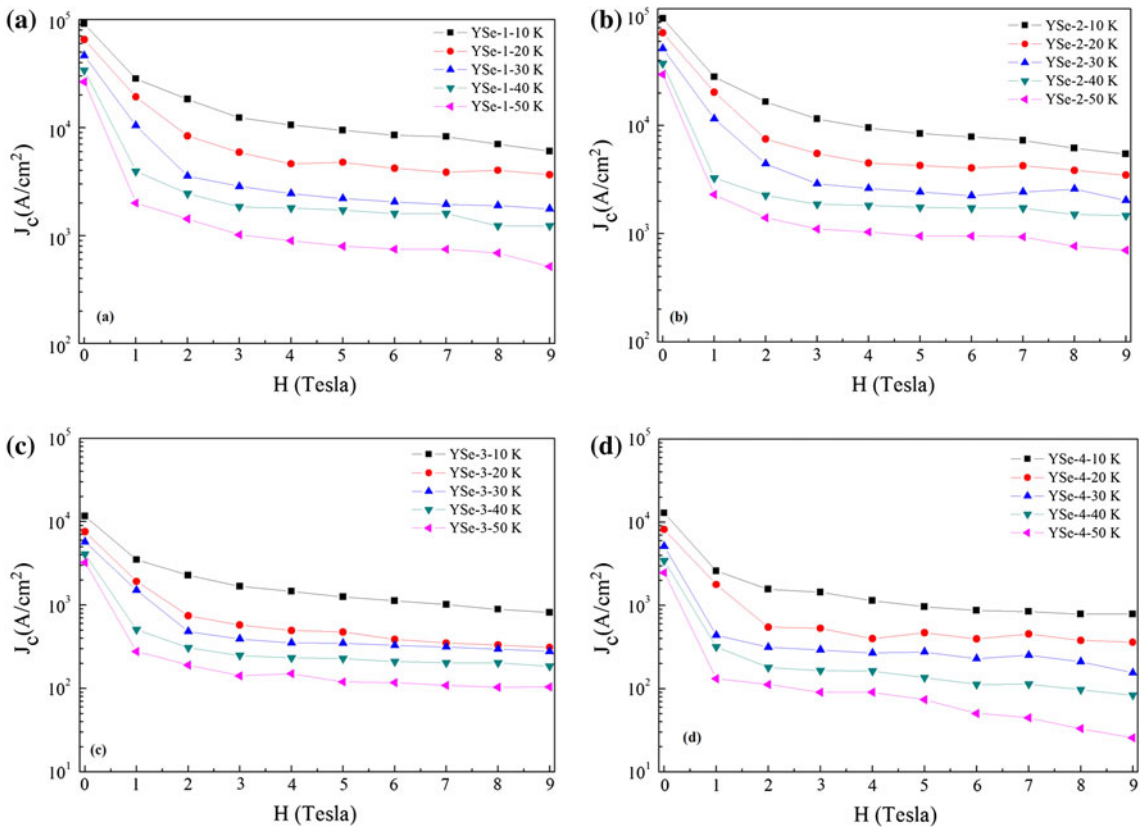

Fig. 8 J_c–H dependence's at 10, 20, 30, 40 and 50 K for the samples fabricated (**a**) 900 °C, (**b**) 920 °C, (**c**) 940 °C and (**d**) 960 °C for 24 h under oxygen atmosphere

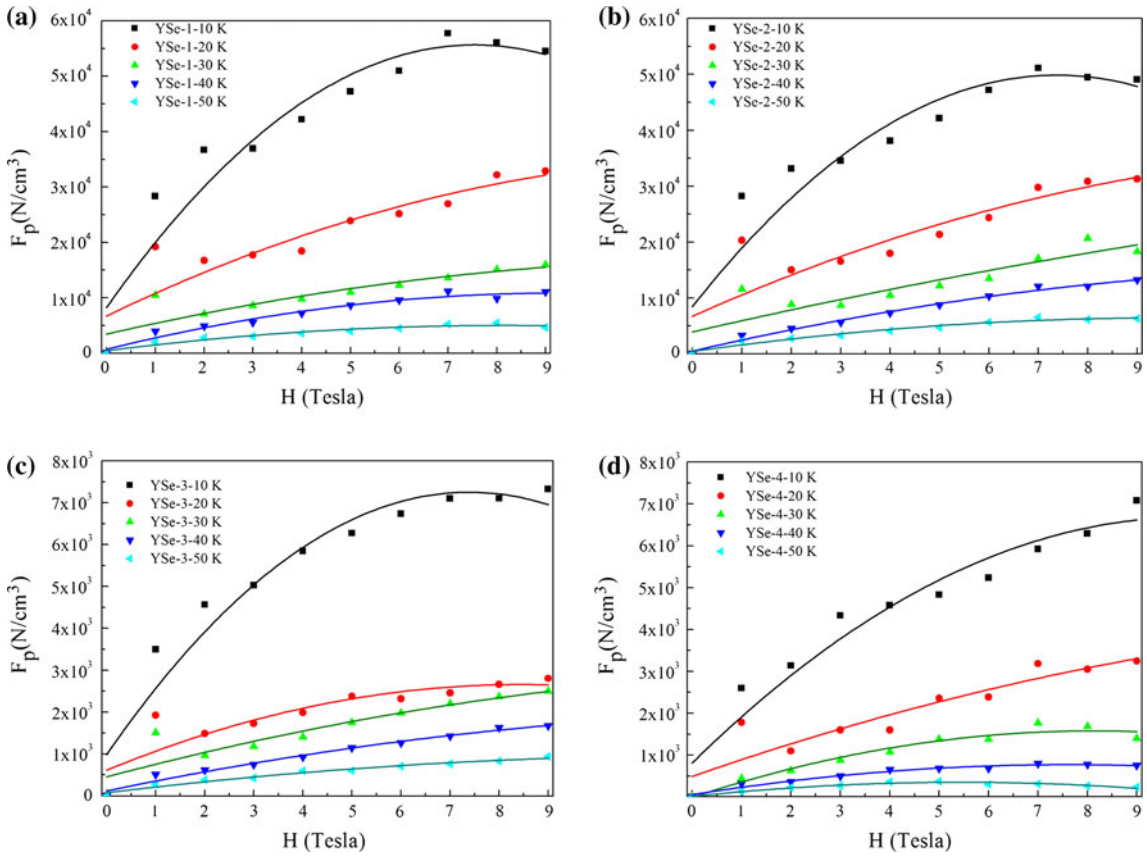

Fig. 9 F_p–H dependence's at 10, 20, 30, 40 and 50 K for the samples fabricated (**a**) 900 °C, (**b**) 920 °C, (**c**) 940 °C and (**d**) 960 °C for 24 h under oxygen atmosphere

grain interacts with only one pinning center. In this state, the bulk F_p has a maximum value, because each pinning center applies a maximal constraint on the FLL [32].

When the number of flux lines is equal to the number of pinning centers which penetrates to the sample at the applied magnetic field, the maximum F_p value is reached. Therefore, the applied field value at the maximum F_p depends strongly on the number of pinning centers penetrating to the samples and the peak value in F_p related to the strength of the basic interactive forces (basic interactive forces are the forces between single, isolated flux lines and individual pinning centers). At the higher fields, there are more flux lines than pinning centers and therefore, a crossover from synchronization can be expected [33].

The grain size in the samples has also an importance on the pinning behavior depending on the applied magnetic fields. A decrease of grain size on the order of the flux lattice constant can cause the vortex channels to overlap, so the average direction of flux motion incorporates a component perpendicular to the grain boundaries. In this case, F_p is much stronger than before and it is necessary to apply higher magnetic fields to break vortex in sample. This causes the peak of F_p to shift toward higher applied magnetic fields [34].

4 Conclusion

$Y_{2/3}Se_{1/3}Ba_2Cu_3O_x$ samples were successfully fabricated using solid state reaction technique. Crystal structure of samples was belonged to Y-123. Superconducting transition temperature was investigated both by R–T and M–T measurement technique. The value of superconducting transition temperature of samples were similar to Y-123 superconductor. The M–H loop and critical current density of samples were investigated and it is found that Se addition and Ba and Cu deficiency increased the J_c value of the samples. The extended Valkov–Khrustalev model was applied to describe the magnetization loops at different temperatures. The behavior of estimated pinning force is argued for the samples.

Acknowledgments The work is supported by Project No. 7 of RAS Program "Quantum physics of condensed matter".

References

1. K. Wu, J.R. Ashburn, C.J. Torng, P.H. Hor, R.L. Meng, L. Gao, Z.J. Huang, Y.Q. Wang, C.W. Chu, Phys Rev Lett **58**, 908–910 (1987)

2. R.J. Cava, J.J. Krajewski, W.F. Peck Jr, B. Battelog, L.W. Rupp Jr, R.M. Fleming, A.C.W.P. James, P. Marsh, Nature **336**, 660–662 (1988)
3. M. Kato, M. Nakanishi, T. Miyano, T. Shimizi, M. Kakihana, K. Kosuge, J Solid State Chem **139**, 266–273 (1998)
4. F. Abbattista, M. Vallino, D. Mazza Mat, Chem Phys **21**, 521–528 (1989)
5. J.-Y. Genoud, T. Graf, G. Triscone, A. Junod, J. Muller, Physica C **192**, 137–146 (1992)
6. J.Y. Juang, M.C. Hsieh, C.W. Luo, T.M. Uen, K.H. Wu, Y.S. Gou, Physica C **329**, 45–50 (2000)
7. M.P. Oomen, M. Leghissa, B. Utz, H.W. Neumuller, Mater Res Soc Symp Proc **3**, 137–139 (2004)
8. L. Jansen, R. Block, Phys A **277**, 183–203 (2000)
9. S. Nakajima, M. Kikuchi, Y. Syono, T. Oku, D. Shindo, K. Hiraga, N. Kobayashi, H. Iwasaki, Y. Muto, Physica C **158**, 471–476 (1989)
10. H. Schmid, T. Burkhardt, B.N. Sun, J.P. Rivera, Physica C **157**, 555–560 (1989)
11. T. Yoshitika, W. Hattori, S. Tahara, J Appl Phys **84**, 2176–2180 (1998)
12. A.L. Vasillev, G.V. Tendeloo, Y. Boikov, E. Olsson, Z. Ivanov, Supercond Sci Technol **10**, 356–365 (1997)
13. W. Hattori, T.Y. Yoshitake, S. Tahara, IEEE Trans Appl Supercond **11**, 3205–3208 (2001)
14. P. Schneider, G. Linker, R. Schneider, J. Reiner, J. Geerk, Physica C **266**, 271–277 (1996)
15. M.D. Bethesda, *Hazardous substances data bank* (National Library of Medicine, Denver, CO, 1996). Micromedex
16. A. Slebarski, A. Chelkowski, J. Jelonek, A. Kasprzyk, Solid State Commun **73**, 515–517 (1990)
17. S. Kambe, M. Kawai, Jpn J Appl Phys **27**, L2342–L2344 (1988)
18. H. Shaked, P.M. Keane, J.C. Rodriguez, *Crystal structures of the high-Tc superconducting copper-oxides* (Elsevier, Amsterdam, 1994)
19. M.B. Turkoz, S. Nezir, A. Varilci, G. Yildirim, M. Akdogan, C. Terzioglu, J Mater Sci Mater Electron **24**, 1536–1545 (2013)
20. M.B. Turkoz, S. Nezir, C. Terzioglu, A. Varilci, G. Yildirim, J Mater Sci Mater Electron **24**, 896–905 (2013)
21. C.P. Poole, *Superconductivity* (Acedemic Press, London, 1995)
22. S. Altin, M.A. Aksan, Y. Balci, M.E. Yakinci, J Supercond Nov Magn **22**, 775–784 (2009)
23. M. Oussena, P.A.J. de Groot, A. Marshall, J.S. Abell, Phys Rev B **49**, 1484–1487 (1994)
24. Y.G. Xiao, B. Yin, J.W. Li, Z.X. Zhao, X.K. Fu, H.T. Ren, L. Xiao, J Appl Phys **81**, 2308–2314 (1997)
25. D.A. Balaev, A.A. Dubrovskiy, K.A. Shaikhutdinov, S.I. Popkov, D.M. Gokhfeld, YuS Gokhfeld, M.I. Petrov, JETP **108**, 241–248 (2009)
26. D.M. Gokhfeld, D.A. Balaev, M.I. Petrov, S.I. Popkov, K.A. Shaykhutdinov, V.V. Valkov, J Appl Phys **109**, 033904 (2011)
27. V.V. Val'kov, B.P. Khrustalev, JETP **80**, 680–685 (1995)
28. D.X. Chen, R.W. Cross, A. Sanchez, Cryogenics **33**, 695–703 (1993)
29. C.P. Bean, Phys Rev Lett **8**, 250–253 (1962)
30. M. Cai, M.H. Fang, X.J. Zhang, Z.K. Jiao, Q.R. Zhang, X.S. Rong, B.R. Zhao, Phys Stat Sol a **147**, 221–227 (1995)
31. W.C. Chan, C.H. Chiang, Y.J. Hsu, Cryogenics **50**, 292–294 (2010)
32. M. Konczykowski, Y. Yeshurun, L. Klein, E.R. Yacoby, N. Chikumoto, V.M. Vinokur, M.V. Feigel'man, J Alloy Compd **195**, 407–410 (1993)
33. P.J. Lee, *Engineering superconductivity* (Willey-Interscience, Canada, 2001)
34. L.D. Cooley, P.J. Lee, IEEE Trans Appl Supercond **11**, 3820–3823 (2001)